


Fe and Cr co-intercalation in 2H-NbS₂ single crystals for realization of perpendicular magnetic anisotropy and large anomalous Hall effect

Shuang Pan,¹ Li Tang,¹ Yuqing Bai,¹ Jiaxuan Tang,¹ Zhishuo Zhang,¹ Bin Chen[✉],¹ Yong Guo,¹ Jie Zhu[✉],² Guizhou Xu[✉],^{1,*} and Feng Xu^{1,†}

¹*School of Materials Science and Engineering, Nanjing University of Science and Technology, Nanjing 210094, People's Republic of China*

²*State Key Laboratory for Advanced Metals and Materials, University of Science and Technology Beijing, Beijing 100083, People's Republic of China*

 (Received 25 November 2022; revised 9 February 2023; accepted 6 March 2023; published 17 March 2023)

Recently, many interesting magnetic and electrical properties have been demonstrated in transition-metal intercalated 2H-NbS₂/TaS₂ layered single crystals. In this work, single crystals of Cr and Fe co-intercalated 2H-NbS₂, with the compositions of (Cr_{1-x}Fe_x)_{1/3}NbS₂ ($x = 0.0-1.0$), are successfully grown and their magnetic and transport properties are systematically studied. With increasing Fe content, the magnetic transition temperature continually decreases from 117 to 37 K, and the magnetic coupling transforms from ferromagnetic to antiferromagnetic. Importantly, a rotation of the magnetic easy axis occurs in this process, with perpendicular magnetocrystalline anisotropy and considerable coercive field achieved in the $x = 0.13-0.66$ compounds. Both $x = 0.33$ and $x = 0.50$ exhibit relatively low carrier concentration, stable anomalous Hall effect, and butterfly-shape magnetoresistance. Notably, large anomalous Hall conductivity is identified in $x = 0.50$, whose origin is discussed from the calculated electronic structures. The realization of perpendicular anisotropy and large anomalous Hall conductivity in this two-dimensional ferromagnetic system can facilitate their future application in spintronic devices.

DOI: [10.1103/PhysRevMaterials.7.034407](https://doi.org/10.1103/PhysRevMaterials.7.034407)

I. INTRODUCTION

Two-dimensional (2D) van der Waals (vdW) ferromagnetic (FM) materials have been widely studied in the past few years due to their unique crystal structure; rich chemical intercalation; and intriguing magnetic, electronic, and optical properties [1–6]. The stereotypical 2D ferromagnetic materials, such as CrI₃ [7–9], Cr₂Ge₂Te₆ [10], and Fe₃GeTe₂ [11,12], have exhibited fascinating properties, while the tunability of the magnetism in these systems is limited by their relatively fixed stoichiometry. Another large family of 2D magnetic materials consists of the 3d atom intercalated transition-metal dichalcogenides (TMDs), where diversified magnetic states have been observed when adjusting the type or proportion of the intercalated elements and host lattice [13–15]. For instance, Cr_{1/3}NbS₂ is a monoaxial chiral magnetic material with in-plane anisotropy, which exhibits helical magnetism and a chiral soliton lattice (CSL) [16,17]. This novel magnetic structure is also successively found in the in-plane easily magnetized Mn_{1/3}NbS₂ and Cr_{1/3}TaS₂ [18,19]. On the other hand, Fe_{1/3}NbS₂ exhibits an antiferromagnet state with anisotropic magnetoresistance, where the magnetic state can be switched by an in-plane electrical current [20–22]. As previously reported, when Nb is replaced by Ta, Fe_xTaS₂ becomes a ferromagnet with strong perpendicular magnetic anisotropy (PMA) [23,24], significant coercive force (H_c) [25,26], and large magnetoresistance (MR) [27–29]. Based on the above facts, we note that Cr intercalation mainly leads to

in-plane anisotropy with a chiral magnetic lattice, while most Fe intercalation brings out-of-plane anisotropy, even in the antiferromagnetic (AFM) ones. Hence, one natural question is that if Cr and Fe are codoped into the layered MS₂, how would the anisotropy and magnetic order be tuned? Is it possible to realize a new 2D ferromagnet with PMA, which is favored for spintronic devices?

Therefore, in this work, Fe and Cr elements are simultaneously intercalated into 2H-NbS₂, and the whole intercalation concentration is controlled at 1/3 to maintain the superlattice structure of M_{1/3}NbS₂ ($M = \text{Fe, Cr, Mn, etc.}$). We find that co-intercalation can not only generate a perpendicular magnetic anisotropy in the intermediate components, but also produces an inherently hard magnetic phase with considerable coercivity. Magnetotransport investigation shows a large anomalous Hall conductivity (AHC) and low carrier concentration at $x = 0.50$, which is comparable to the performance of the Fe_xTaS₂ under the same conditions [30]. Therefore, co-intercalation provides an alternative and feasible idea for tuning the performance of TMDs.

II. EXPERIMENTAL AND CALCULATION DETAILS

Single crystals were obtained by the chemical vapor transfer method (CVT) using a dual-temperature zone furnace. A mixture of M ($M = \text{Cr or/and Fe}$), Nb, and S at the desired ratio was prepared and sealed in a vacuum quartz tube for presintering, noting that the Fe content exceeded the stoichiometry by about 20%, in order to compensate for the loss of iron during calcination. The tube with the raw material was heated to 800 °C in a muffle furnace for 6 h and held for 5

*gzxu@njust.edu.cn

†xufeng@njust.edu.cn

TABLE I. Collected data for the samples including sample name and measured composition [x in $(\text{Cr}_{1-x}\text{Fe}_x)_{1/3}\text{NbS}_2$].

| Sample name | Measured composition (EDS) |
|-------------|--|
| $x = 0.0$ | $\text{Cr}_{0.33\pm 0.01}\text{NbS}_{1.97\pm 0.03}$ |
| $x = 0.13$ | $(\text{Cr}_{0.81\pm 0.02}\text{Fe}_{0.13\pm 0.01})_{1/3}\text{NbS}_{1.98\pm 0.02}$ |
| $x = 0.23$ | $(\text{Cr}_{0.79\pm 0.01}\text{Fe}_{0.23\pm 0.007})_{1/3}\text{NbS}_{1.93\pm 0.03}$ |
| $x = 0.33$ | $(\text{Cr}_{0.69\pm 0.03}\text{Fe}_{0.33\pm 0.01})_{1/3}\text{NbS}_{1.92\pm 0.08}$ |
| $x = 0.50$ | $(\text{Cr}_{0.44\pm 0.01}\text{Fe}_{0.49\pm 0.02})_{1/3}\text{NbS}_{1.94\pm 0.05}$ |
| $x = 0.66$ | $(\text{Cr}_{0.30\pm 0.04}\text{Fe}_{0.66\pm 0.02})_{1/3}\text{NbS}_{1.99\pm 0.01}$ |
| $x = 1.0$ | $\text{Fe}_{0.31\pm 0.008}\text{NbS}_{1.96\pm 0.02}$ |

days; then the whole furnace was cooled to room temperature to form polycrystalline powder with a metallic luster. The presintered powder was sealed in a vacuum quartz tube with iodine as a transfer agent, and was heated at 450 °C for 1 day in the dual-temperature zone furnace. Then it was heated at 950 °C in the raw material zone and 850 °C in the growth zone for 5 days. Finally, hexagonal $(\text{Cr}_{1-x}\text{Fe}_x)_{1/3}\text{NbS}_2$ single crystals with shining surfaces were obtained. It is found that this family of materials is not easily degraded and can remain stable in the air for a long time. Different pieces from each batch of samples also exhibit stably repeated properties. The compositions were determined by energy dispersive spectroscopy (EDS) with a scanning electron microscope (SEM, FEI Quanta 250 F). It should be mentioned that the composition of Cr, Fe, and S in the single crystals deviates a little from the desired ratio, within the range of 0.007–0.08, which has also been mentioned in similar systems [20,31]. The values of the exact compositions in this study are shown in Table I. For simplicity, we applied the nominal compositions in the description of different components.

The crystal structure and orientation were acquired by x-ray diffraction (XRD) using Cu $K\alpha$ radiation on a Bruker-AXS D8 Advance at room temperature. Temperature- and field-dependent magnetization was measured along the in-plane ($H\parallel ab$) and out-of-plane ($H\perp ab$) directions in a magnetic property measurement system (MPMS, Quantum Design). The magnetoresistance (MR) and Hall effect measurements were performed by a standard four-probe method using a physical property measurement system (PPMS, Quantum Design).

First principles calculations were performed with the projector augmented wave (PAW) method, as implemented in the Vienna *ab initio* simulation package (VASP) [32,33]. The exchange correlation effect was treated with the generalized gradient approximation (GGA) function in the form of Perdew-Burke-Ernzerhof (PBE) parametrization. The static self-consistency calculations and density of states (DOS) integrations were carried out on a k grid of $9 \times 9 \times 9$, with the cutoff energy of 400 eV for the plane wave basis set. The orbital magnetic moment was calculated by switching on the spin-orbital coupling.

III. RESULTS AND DISCUSSION

According to reports in the literature [34–36], $M_{1/3}\text{NbS}_2$ ($M = \text{Cr}$ or/and Fe) possesses a noncentrosymmetric hexagonal structure ($P6_322$), where the intercalant elements occupy

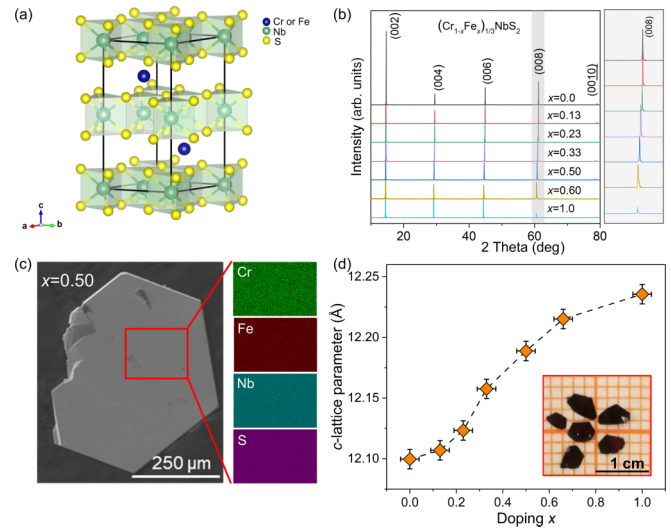


FIG. 1. (a) Crystal structure of bulk $M_{1/3}\text{NbS}_2$ ($M = \text{Cr}$ or/and Fe). Blue, green, and yellow balls represent Cr or Fe, Nb, and S atoms, respectively. (b) XRD patterns of $(\text{Cr}_{1-x}\text{Fe}_x)_{1/3}\text{NbS}_2$ single-crystal thin plates, along with (008) enlarged diffraction peaks. (c) The morphology and elemental distribution of sample $x = 0.50$ single crystal scanned by SEM. (d) The c -lattice parameters for $(\text{Cr}_{1-x}\text{Fe}_x)_{1/3}\text{NbS}_2$ plotted with Fe doping content. Inset: Optical image of $(\text{Cr}_{1-x}\text{Fe}_x)_{1/3}\text{NbS}_2$ single crystals.

the octahedral position between the triangular prismatic, and six S ions surround one Nb ion [Fig. 1(a)]. Our XRD patterns for all the intercalated samples are consistent with this structure, and only the single-crystalline (00 l) orientation is observed [Fig. 1(b)], indicating that the Cr and Fe can compatibly occupy the same site and the single-crystalline samples are grown along the c axis. The peak position is slightly shifted with the different proportions of Cr and Fe, while the overall lattice constant changes slightly (from 12.10 to 12.24 Å), as seen in the extracted c parameter in Fig. 1(d). It exhibits a systematic expansion of the interlayer spacing with Fe substitution of Cr, owing to the larger ionic radii of the Fe atom. The SEM image and elemental mapping of all samples demonstrate a near hexagonal structure and uniform elemental distribution, as exemplified in $x = 0.50$ [Fig. 1(c)]. The single crystals overall have a maximum lateral dimension of 3 mm and thickness of around 30–60 μm [in the inset of Fig. 1(d)].

The temperature-dependent magnetization (M - T) curves of $(\text{Cr}_{1-x}\text{Fe}_x)_{1/3}\text{NbS}_2$ ($x = 0.0$ – 1.0) single crystals are measured for both in-plane ($H\parallel ab$) and out-of-plane ($H\perp ab$) directions with a field-cooling sequence ($\mu_0 H = 0.05$ T). As shown in Figs. 2(a) and 2(e), the magnetic transitions of pure $\text{Cr}_{1/3}\text{NbS}_2$ and $\text{Fe}_{1/3}\text{NbS}_2$ are reflected with the Curie temperature (T_c) and Néel temperature (T_N) of 117 and 37 K, respectively, consistent with the literature data [37–39]. In addition, the comparison of the magnetization magnitude in different directions indicates the expected easy ab -plane magnetization in $\text{Cr}_{1/3}\text{NbS}_2$ [40] and easy c -axis magnetization in $\text{Fe}_{1/3}\text{NbS}_2$ [41]. With the increasing substitution of Cr by Fe, the magnetic transition temperature decreases monotonically, accompanied by the emergence of some low-temperature transitions. Figure 2(b) shows a clear FM transition at $T_c = 120$ K

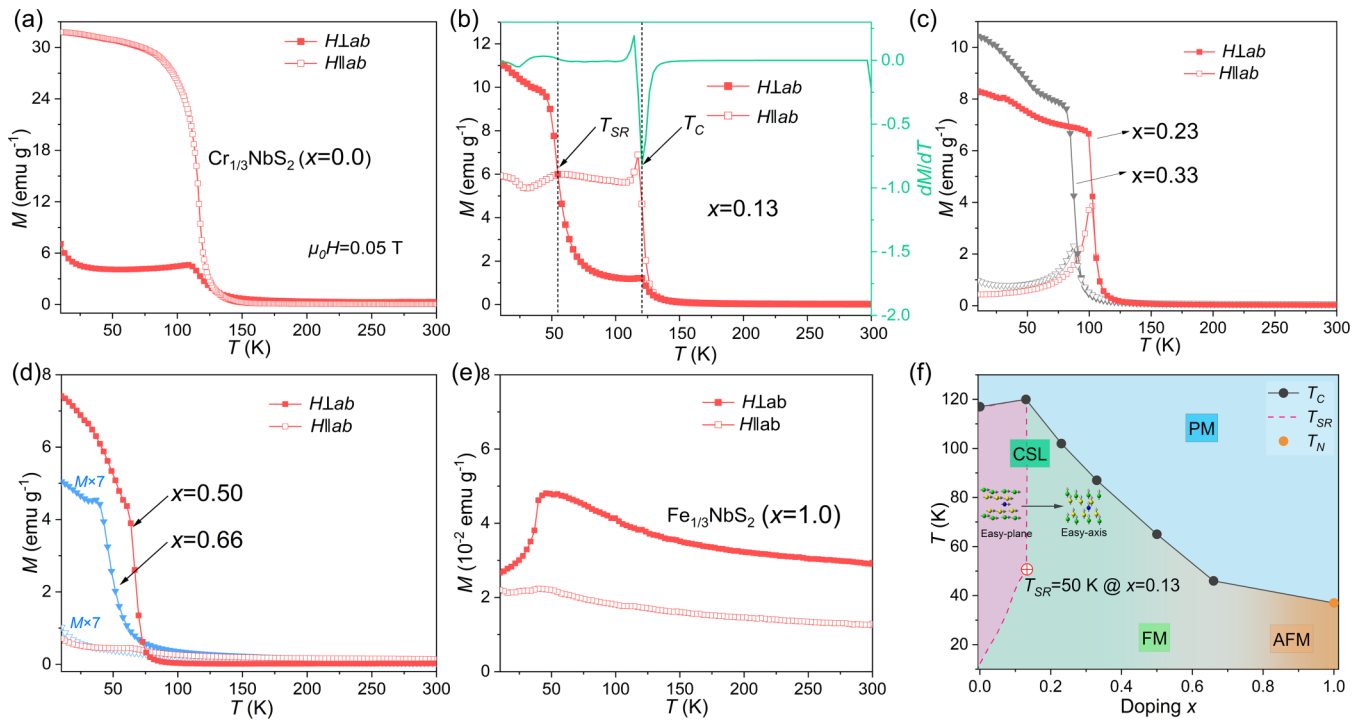


FIG. 2. [(a)–(e)] Temperature-dependent magnetization M - T curves of $(\text{Cr}_{1-x}\text{Fe}_x)_{1/3}\text{NbS}_2$ ($0.0 \leq x \leq 1.0$) measured in field-cooling process with $\mu_0 H = 0.05$ T for $H \perp ab$ (solid symbols) and $H \parallel ab$ (open symbols), respectively. (f) Doping-temperature magnetic phase diagram of $(\text{Cr}_{1-x}\text{Fe}_x)_{1/3}\text{NbS}_2$.

for $x = 0.13$ and a spin-reorientation-like transition at $T_{SR} = 55$ K, below which the magnetization along the c -axis becomes larger than that along the ab plane, indicating the easy spin axis reorients from in plane to out of plane. With increasing Fe content, as shown in Fig. 2(c), of $x = 0.23$ and 0.33 , the FM transition temperature continually drops. In addition, we observe a cusp around T_c for $H \parallel ab$ in $x = 0.13$ – 0.33 , which is a characteristic feature of the chiral soliton lattice (CSL), as comprehensively studied in $\text{Cr}_{1/3}\text{NbS}_2$ [38,42,43]. The cusp disappears for $x \geq 0.50$ [Fig. 2(d)], where the curve shows pure FM states for $H \perp ab$, indicating the stability of CSL is broken at this critical point. The magnetization in $x = 0.66$ becomes rather small, implying the transformation trend from the FM to the AFM state. Figure 2(f) summarizes the temperature- and composition-dependent phase diagram for $(\text{Cr}_{1-x}\text{Fe}_x)_{1/3}\text{NbS}_2$ samples. The magnetization transition temperatures are extracted using the M - T curves. It can be seen that with increasing Fe content, the CSL state in the pristine $\text{Cr}_{1/3}\text{NbS}_2$ becomes less stable, and the weakened FM exchange interaction tends to suppress the magnetic transition temperature [34], leading to the decrease of the T_c , and finally transforms to the AFM state of $\text{Fe}_{1/3}\text{NbS}_2$. Simultaneously, the magnetization easy axis also rotates, which will be investigated in detail with further measurements in the following.

The field-dependent magnetization (M - H) curves along both $H \parallel ab$ and $H \perp ab$ are measured at 10 K for all samples (except for $x = 1.0$, which is AFM). As shown in Fig. 3(a), the easy magnetization along the ab plane is only observed for $x = 0.0$, i.e., the $\text{Cr}_{1/3}$ sample. It obviously turns to the out-of-plane direction for $x = 0.13$ – 0.50 , and $x = 0.66$ reveals nonsaturating behavior that indicates antiferromagnetic

exchange interaction. Since the measured magnetization is rather weak for these tiny two-dimensional samples, the saturation magnetizations M_s sometimes cannot match well in the two directions of the ab plane and c axis. In the meantime, the H_c appears and increases until it reaches a maximum at $x = 0.50$ and 0.66 , where part of the magnetic moment flips with increasing Fe content to form more AFM phases, leading to a strong pinning effect at the interface between the AFM and original FM magnetic domains, as in $\text{Fe}_{0.25}\text{TaS}_2$ [26]. The evolution of the remanence (M_r) and H_c are summarized in Fig. 3(b), which proves that $x = 0.33$ and 0.50 own good, hard magnetic properties. The resulting out-of-plane anisotropy is thought to be related to the non-negligible orbital magnetic moment of intercalated Fe ions, as discussed in Refs. [44,45] and our later calculations. In addition, to inspect the CSL evolution with increasing Fe content, we measure denser M - H curves of three characteristic components along the ab plane with smaller field steps [Fig. 3(c)]. It is found that at $x = 0.0$ and 0.13 an intermediate state is observed before transforming to the FM state, which represents the unique chiral soliton lattice state, having been reported in $\text{Cr}_{1/3}\text{NbS}_2$ [19,46]. However, it should be noted that at $x = 0.13$, the dense M - H is measured at $T = 100$ K, which is above the spin reorientation transition and the easy magnetization is still along the ab plane. This transition has been mentioned before when investigating the M - T curves and is further confirmed in the detailed M - H curves for various temperatures in Fig. 3(d). Therefore, $x = 0.13$ can be seen as a critical composition where the easy-spin axis starts to rotate and CSL could persist at a certain temperature. When the easy magnetization direction totally turns to the c axis, the CSL state is suppressed,

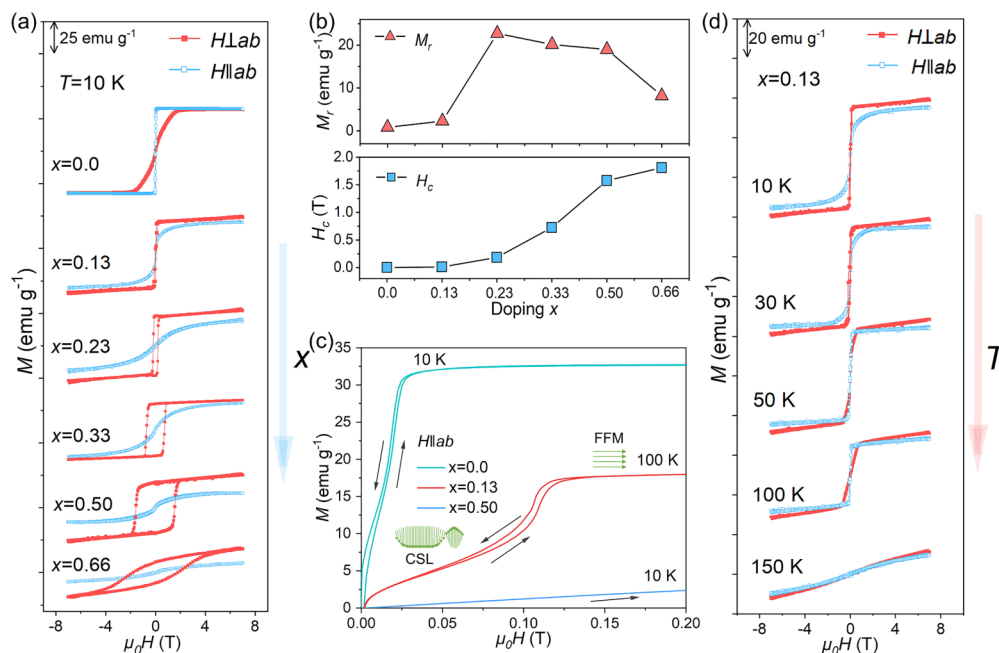


FIG. 3. (a) M - H curves along $H \perp ab$ and $H \parallel ab$ for various compositions of $0.0 \leq x \leq 0.66$ at $T = 10$ K. (b) The extracted remanence (M_r) and coercive field (H_c) values of $(\text{Cr}_{1-x}\text{Fe}_x)_{1/3}\text{NbS}_2$. (c) M - H curves at a dense magnetic field variation for three components, $x = 0.0$ (at 10 K), 0.13 (at 100 K), and 0.50 (at 10 K). (d) M - H curves of $x = 0.13$ along $H \perp ab$ and $H \parallel ab$ at different temperatures (10, 30, 50, 100, and 150 K).

as displayed in $x = 0.50$ of Fig. 3(c). Therefore, the spin-axis reorientation is realized by substituting Fe with Cr in this two-dimensional material host, and the out-of-plane anisotropy can facilitate their application in the perpendicular spintronic devices.

To further investigate the electrical properties of these compositions with out-of-plane anisotropy, the temperature-dependent Hall effect and magnetoresistance are measured for $x = 0.33$ and 0.50 samples. As seen in Figs. 4(a) and 4(b), anomalous Hall effect (AHE) is observed in both $x = 0.33$ and 0.50 below T_c , and large hysteresis is presented at low temperature, consistent with the M - H behavior. It is noted that at high field, the behaviors of $x = 0.33$ and 0.50 are different; the former has a negative slope while the latter has a positive one. Since the anomalous Hall signal can be empirically expressed as $\rho_{xy} = \rho_{xy}^o + \rho_{xy}^A = \mu_0(R_0H + R_sM)$, where R_0 , R_s are the ordinary and anomalous Hall coefficient, respectively, we extract the anomalous Hall resistivity ρ_{xy}^A with the intercept of the high-field linear fitting and the ordinary coefficient R_0 with the slope of it. Further, the AHC is calculated with the relation of $\sigma_{xy}^A = \rho_{xy}^A / [(\rho_{xy}^A)^2 + \rho_{xx}^2]$, where ρ_{xx} is zero field resistivity, and the carrier concentration is evaluated with $n = 1/|eR_0|$ (e is the charge of the electron). The calculated values of σ_{xy}^A and n for $x = 0.33$ and 0.50 are summarized in Figs. 4(c) and 4(d), together with some literature data from similar systems. It is found that $x = 0.50$ has a significantly large magnitude of AHC, ranging from $162 \Omega^{-1} \text{cm}^{-1}$ (50 K) to $281 \Omega^{-1} \text{cm}^{-1}$ (10 K), which can be compared to the value of the ferromagnetic $\text{Fe}_{0.3}\text{TaS}_2$ [30], while in $x = 0.33$, the AHC shows the small value of $46 \Omega^{-1} \text{cm}^{-1}$ (10 K) to $23 \Omega^{-1} \text{cm}^{-1}$ (50 K), like the Co based or $\text{Fe}_{1/4}$ intercalated Nb/Ta S_2 [25,30,47–49]. The carrier concentration n of $x = 0.50$ is on the order

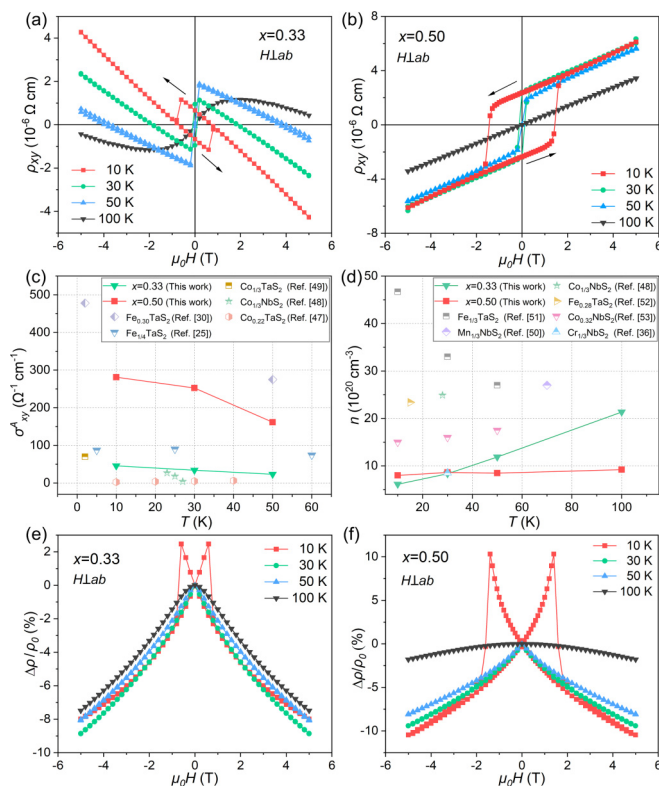


FIG. 4. [(a), (b)] Hall resistivity of $x = 0.33$ and 0.50 with $H \perp ab$ at different temperatures. (c) σ_{xy}^A vs T plot for samples in this work and other similar systems [25,30,47–49]. (d) n vs T plot for samples in this work and other systems [36,48,50–53]. [(e), (f)] MR for samples of $x = 0.33$ and 0.50 with $H \perp ab$ at different temperatures.

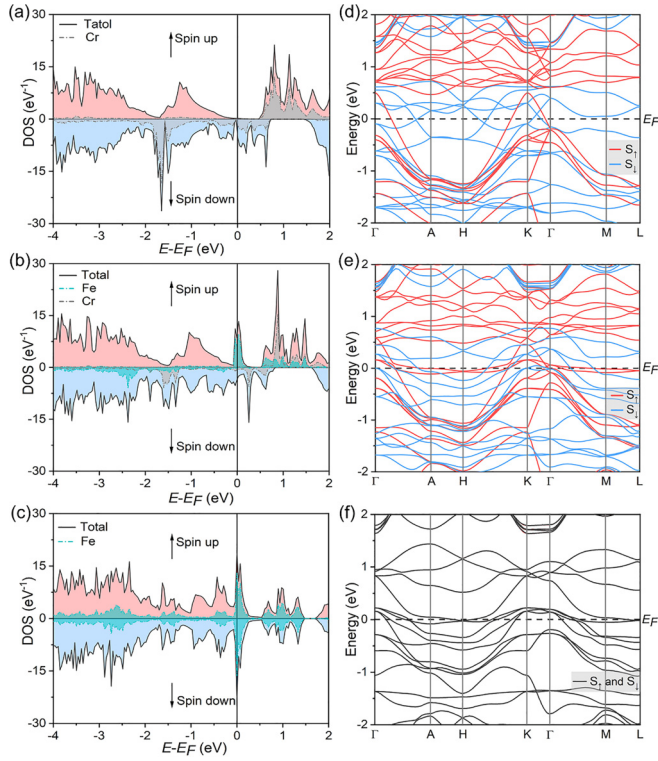


FIG. 5. [(a)–(c)] Spin and atomic resolved density of states (DOS) for ferromagnetic $\text{Cr}_{1/3}\text{NbS}_2$, $(\text{Cr}_{0.50}\text{Fe}_{0.50})_{1/3}\text{NbS}_2$, and antiferromagnetic $\text{Fe}_{1/3}\text{NbS}_2$, respectively. The red and blue areas correspond to total DOS in spin-up and spin-down directions, respectively; the gray and green areas correspond to the partial DOS of Cr and Fe atoms, respectively. [(d)–(f)] are their corresponding band structures. As $\text{Fe}_{1/3}\text{NbS}_2$ is antiferromagnetic, the spin-up band is superposed with that of spin down.

of 10^{20} cm^{-3} , bringing large carrier mobility $\mu = \sigma_{xx}/ne$ (σ_{xx} is longitudinal conductivity at zero field) of about $50\text{--}80 \text{ cm}^2 \text{ V}^{-1} \text{ s}^{-1}$. The n in sample $x = 0.33$ is a bit larger, ranging from 6×10^{20} (10 K) to $21 \times 10^{20} \text{ cm}^{-3}$ (100 K), and the corresponding carrier mobility drops quickly from 74.53 to $5.50 \text{ cm}^2 \text{ V}^{-1} \text{ s}^{-1}$. The order of their carrier concentrations is close to $\text{Cr}_{1/3}\text{NbS}_2$ ($n = 8.53 \times 10^{20} \text{ cm}^{-3}$ at 30 K [36]), but the values are smaller than those of other single-atom intercalated Nb/TaS₂ ranging from 1.5×10^{21} to $4.6 \times 10^{21} \text{ cm}^{-3}$ [48,50–53], which can be attributed to the low density of states at the Fermi level [(Fig. (5)]. The comparatively large carrier mobility and anomalous Hall conductivity in $x = 0.50$ make it attractive in building spintronic devices based on 2D ferromagnetic material.

Figures 4(e) and 4(f) show the MR of them at various temperatures. The overall MR of $x = 0.33$ and 0.50 are both negative upon a large external field, but at low temperature (here $T = 10 \text{ K}$), the MR first grows to a maximum value during increasing field, then drops sharply within a very narrow magnetic field interval, making a butterfly double-peak shape at low fields after one cyclic period of magnetic field sweep. This is in coincidence with the hard M - H behavior of $x = 0.33$ and 0.50 at $T = 10 \text{ K}$ [(see Fig. 3(a)], which is correlated to the domain wall pinning. The jump magnitude of $\Delta\rho/\rho$ in the low-field metastable state can reached 2.5% (at

TABLE II. The structure parameters (in Å) used in the calculation and the calculated spin and orbital magnetic moments (in μ_B) for $\text{Cr}_{1/3}\text{NbS}_2$, $(\text{Cr}_{0.50}\text{Fe}_{0.50})_{1/3}\text{NbS}_2$, and $\text{Fe}_{1/3}\text{NbS}_2$.

| | a (Å) | c (Å) | $m_{\text{spin}}(\mu_B)$ | $m_o(\mu_B)$ |
|--|--------------------|---------------------|--------------------------|--------------|
| $\text{Cr}_{1/3}\text{NbS}_2$ | 5.730 ^a | 12.110 ^a | 2.965 | 0.029 |
| $(\text{Cr}_{0.50}\text{Fe}_{0.50})_{1/3}\text{NbS}_2$ | 5.745 | 12.144 | 2.848 (Cr) | 0.018 (Cr) |
| | | | 2.994 (Fe) | 0.046 (Fe) |
| $\text{Fe}_{1/3}\text{NbS}_2$ (AFM) | 5.761 ^a | 12.178 ^a | 3.104 | 0.186 |

^aFrom Ref. [45].

0.6 T) and 10.4% (at 1.4 T), respectively. At $H > H_c$ and other temperatures without coercivity, the spin-related scattering makes the $\Delta\rho/\rho$ descend with the increasing field, reaching a moderate negative MR value of $\sim 10\%$ at 5 T.

Finally, the magnetic moments and electronic structures of $(\text{Cr}_{1-x}\text{Fe}_x)_{1/3}\text{NbS}_2$ ($x = 0.0, 0.50, \text{ and } 1.0$) are calculated to elaborate the evolution of the magnetic and transport properties. We have applied the supercell that contains six primitive cells of $\text{M}_{1/3}\text{NbS}_2$ in the calculation, so for the middle composition of $x = 0.50$, one Cr atom and one Fe atom are included in the cell. For $x = 0.0$ and 0.50 , the initial state is set as FM, while $x = 1.0$ is set as the AFM state, based on the experimental result. As seen in Table II, The lattice parameters for $x = 0.0$ and 1.0 are selected as the experimental ones [45], while for $x = 0.50$, the lattice parameter is obtained by linear interpolation of $x = 0.0$, for which the c parameter is slightly lower than our measured ones. The calculated spin moments (m_{spin}) of Cr and Fe are both close to $3 \mu_B$, while the orbital magnetic moment (m_o) of Fe is $0.186 \mu_B$ (in $\text{Fe}_{1/3}\text{NbS}_2$), obviously much larger than that of the Cr atom ($0.029 \mu_B$ in $\text{Cr}_{1/3}\text{NbS}_2$), which is originated from the unquenched orbital occupation of Fe^{2+} compared to Cr^{3+} , as analyzed in Ref. [34]. Even in the middle composition of $x = 0.50$, the m_o of Fe is still larger than that of the Cr atom. This considerable m_o can cause a large spin-orbit interaction and magnetocrystalline anisotropy energy involving $\Delta\vec{L} \cdot \vec{S}$ [44], resulting in the reorientation of the spin axis in the series of our samples.

Figure 5 shows the density of states (DOS) and band structure of $(\text{Cr}_{1-x}\text{Fe}_x)_{1/3}\text{NbS}_2$ ($x = 0.0, 0.50, \text{ and } 1.0$). It is worth noting that FM $\text{Cr}_{1/3}\text{NbS}_2$ reveals a nearly half-metallic magnetism, with only one band of spin-down channel crossing the Fermi level (E_F), which causes the low carrier concentration compared with a regular metal [54]. With the insertion of Fe atoms, a large DOS in the spin-up direction is observed at E_F in $x = 0.50$, mainly dominated by Fe states as seen in Fig. 5(b). The enhanced DOS leads to an enhancing carrier concentration [$n_{x=0.50}(10 \text{ K}) > n_{x=0.33}(10 \text{ K})$] and the boosted band cross points can possibly lead to the larger AHC based on the Berry curvature theory, as in the case of $\text{Fe}_{1/3}\text{TaS}_2$ [41]. For the AFM state of $\text{Fe}_{1/3}\text{NbS}_2$, a peak of DOS around E_F is observed in both spin directions [Fig. 5(c)], indicating the instability of linear AFM interaction, in which a field induced formation of complex spin texture has been reported recently [20]. As the spin-up band is superposed with that of spin down [Fig. 5(f)] the AHC of $\text{Fe}_{1/3}\text{NbS}_2$ has vanished due to the fine reversal symmetry.

IV. CONCLUSION

In summary, we successfully synthesized $(\text{Cr}_{1-x}\text{Fe}_x)_{1/3}\text{NbS}_2$ single crystals by co-intercalating Cr and Fe into the vdW gap, where $x = 0.0\text{--}1.0$. We find that with increasing Fe content, the FM state will gradually transform to AFM coupling, accompanied by the lowering of the magnetic transition temperature. Nevertheless, the easy spin axis can reorient from the in-plane to the out-of-plane direction, where the large perpendicular magnetic anisotropy and hard magnetic properties are achieved in the co-intercalated single crystals of $x = 0.23\text{--}0.66$. The samples of $x = 0.33$ and 0.50 also exhibit low carrier density, anomalous Hall effect, and butterfly-shape magnetoresistance at low temperature, where $x = 0.50$ presents a large anomalous Hall conductivity, which is higher compared to most other similar materials. By analyzing the magnetic orbital moments and electronic structures of $(\text{Cr}_{1-x}\text{Fe}_x)_{1/3}\text{NbS}_2$ ($x = 0.0, 0.50, \text{ and } 1.0$) with

first principles calculations, it is found that the large orbital magnetic moments of the Fe atoms are directly responsible for the reorientation of the spin axis, while the increase in band cross points at the Fermi level of $x = 0.50$ leads to a larger anomalous Hall conductivity. We hope that the present methods and results will direct much more attention to this class of layered magnetic materials.

ACKNOWLEDGMENTS

This work is supported by National Natural Science Foundation of China (Grant No. 11604148), the Open Fund of Large Facilities in Nanjing University of Science and Technology, and State Key Lab of Advanced Metals and Materials (Grant No. 2022-Z20).

S.P. and L.T. contributed equally to this work.

-
- [1] K. S. Burch, D. Mandrus, and J. G. Park, *Nature (London)* **563**, 47 (2018).
- [2] Y. C. Du, G. Qiu, Y. X. Wang, M. W. Si, X. F. Xu, W. Z. Wu, and P. D. Ye, *Nano Lett.* **17**, 3965 (2017).
- [3] X. Wang, Z. Song, W. Wen, H. Liu, J. Wu, C. Dang, M. Hossain, M. A. Iqbal, and L. Xie, *Adv. Mater.* **31**, 1804682 (2019).
- [4] A. Avsar, H. Ochoa, F. Guinea, B. Özyilmaz, B. J. van Wees, and I. J. Vera-Marun, *Rev. Mod. Phys.* **92**, 021003 (2020).
- [5] Y. Liu and Q. Shao, *ACS Nano* **14**, 9389 (2020).
- [6] S. Husain, R. Gupta, A. Kumar, P. Kumar, N. Behera, R. Brucas, S. Chaudhary, and P. Svedlindh, *Appl. Phys. Rev.* **7**, 041312 (2020).
- [7] B. Huang, G. Clark, E. Navarro-Moratalla, D. R. Klein, R. Cheng, K. L. Seyler, D. Zhong, E. Schmidgall, M. A. McGuire, D. H. Cobden, W. Yao, D. Xiao, P. Jarillo-Herrero, and X. Xu, *Nature (London)* **546**, 270 (2017).
- [8] H. H. Kim, B. Yang, T. Patel, F. Sfigakis, C. Li, S. Tian, H. Lei, and A. W. Tsen, *Nano Lett.* **18**, 4885 (2018).
- [9] Z. Sun, Y. Yi, T. Song, G. Clark, B. Huang, Y. Shan, S. Wu, D. Huang, C. Gao, Z. Chen, M. McGuire, T. Cao, D. Xiao, W. T. Liu, W. Yao, X. Xu, and S. Wu, *Nature (London)* **572**, 497 (2019).
- [10] Z. Wang, T. Zhang, M. Ding, B. Dong, Y. Li, M. Chen, X. Li, J. Huang, H. Wang, X. Zhao, Y. Li, D. Li, C. Jia, L. Sun, H. Guo, Y. Ye, D. Sun, Y. Chen, T. Yang, J. Zhang *et al.*, *Nat. Nanotechnol.* **13**, 554 (2018).
- [11] Z. Fei, B. Huang, P. Malinowski, W. Wang, T. Song, J. Sanchez, W. Yao, D. Xiao, X. Zhu, A. F. May, W. Wu, D. H. Cobden, J. H. Chu, and X. Xu, *Nat. Mater.* **17**, 778 (2018).
- [12] Y. Wang, C. Wang, S. J. Liang, Z. Ma, K. Xu, X. Liu, L. Zhang, A. S. Admasu, S. W. Cheong, L. Wang, M. Chen, Z. Liu, B. Cheng, W. Ji, and F. Miao, *Adv. Mater.* **32**, 2004533 (2020).
- [13] M. Naito and S. J. Tanaka, *J. Phys. Soc. Jpn* **51**, 219 (1982).
- [14] S. S. P. Parkin and R. H. Friend, *Philos. Mag. B* **41**, 65 (2006).
- [15] R. H. Friend, A. R. Beal, and A. D. Yoffe, *Philos. Mag.* **35**, 1269 (2006).
- [16] A. A. Aczel, L. M. DeBeer-Schmitt, T. J. Williams, M. A. McGuire, N. J. Ghimire, L. Li, and D. Mandrus, *Appl. Phys. Lett.* **113**, 032404 (2018).
- [17] T. Miyadai, K. Kikuchi, H. Kondo, S. Sakka, M. Arai, and Y. Ishikawa, *J. Phys. Soc. Jpn* **52**, 1394 (1983).
- [18] S. K. Karna, M. Marshall, W. Xie, L. DeBeer-Schmitt, D. P. Young, I. Vekhter, W. A. Shelton, A. Kovacs, M. Charilaou, and J. F. DiTusa, *Nano Lett.* **21**, 1205 (2021).
- [19] C. Zhang, J. Zhang, C. Liu, S. Zhang, Y. Yuan, P. Li, Y. Wen, Z. Jiang, B. Zhou, Y. Lei, D. Zheng, C. Song, Z. Hou, W. Mi, U. Schwingenschlogl, A. Manchon, Z. Q. Qiu, H. N. Alshareef, Y. Peng, and X. X. Zhang, *Adv. Mater.* **33**, 2101131 (2021).
- [20] P. Liu, H. P. Zhu, Q. M. Wu, Y. L. Lu, and Y. Pu, *Appl. Phys. Lett.* **121**, 081901 (2022).
- [21] S. F. Weber and J. B. Neaton, *Phys. Rev. B* **103**, 214439 (2021).
- [22] N. L. Nair, E. Maniv, C. John, S. Doyle, J. Orenstein, and J. G. Analytis, *Nat. Mater.* **19**, 153 (2020).
- [23] C. H. Zhang, Y. Yuan, M. Wang, P. Li, J. W. Zhang, Y. Wen, S. Q. Zhou, and X. X. Zhang, *Phys. Rev. Mater.* **3**, 114403 (2019).
- [24] E. Morosan, H. W. Zandbergen, L. Li, M. Lee, J. G. Checkelsky, M. Heinrich, T. Siegrist, N. P. Ong, and R. J. Cava, *Phys. Rev. B* **75**, 104401 (2007).
- [25] J. G. Checkelsky, M. Lee, E. Morosan, R. J. Cava, and N. P. Ong, *Phys. Rev. B* **77**, 014433 (2008).
- [26] Y. J. Choi, S. B. Kim, T. Asada, S. Park, W. Wu, Y. Horibe, and S. W. Cheong, *EPL* **86**, 37012 (2009).
- [27] Y. Q. Miao, J. J. Guo, Z. Y. Luo, M. Z. Zhong, B. Li, X. G. Wang, Y. Z. Nie, Q. L. Xia, and G. H. Guo, *Front. Phys.* **10**, 847402 (2022).
- [28] W. J. Hardy, C. W. Chen, A. Marcinkova, H. Ji, J. Sinova, D. Natelson, and E. Morosan, *Phys. Rev. B* **91**, 054426 (2015).
- [29] C. W. Chen, S. Chikara, V. S. Zapf, and E. Morosan, *Phys. Rev. B* **94**, 054406 (2016).
- [30] G. Zheng, M. Wang, X. Zhu, C. Tan, J. Wang, S. Albarakati, N. Aloufi, M. Algarni, L. Farrar, M. Wu, Y. Yao, M. Tian, J. Zhou, and L. Wang, *Nat. Commun.* **12**, 3639 (2021).
- [31] M. Nakayama, K. Miwa, H. Ikuta, H. Hinode, and M. Wakihara, *Chem. Mater.* **18**, 4996 (2006).
- [32] G. Kresse and J. Furthmüller, *Comput. Mater. Sci.* **6**, 15 (1996).
- [33] P. E. Blochl, *Phys. Rev. B* **50**, 17953 (1994).
- [34] L. S. Xie, S. Husremovic, O. Gonzalez, I. M. Craig, and D. K. Bediako, *J. Am. Chem. Soc.* **144**, 9525 (2022).

- [35] F. Hulliger and E. Pobitschka, *J. Solid State Chem.* **1**, 117 (1970).
- [36] D. A. Mayoh, J. Bouaziz, A. E. Hall, J. B. Staunton, M. R. Lees, and G. Balakrishnan, *Phys. Rev. Res.* **4**, 013134 (2022).
- [37] X. Li, Z. F. Li, H. Li, Y. Yao, X. K. Xi, Y. C. Lau, and W. H. Wang, *Appl. Phys. Lett.* **120**, 112408 (2022).
- [38] H. Han, L. Zhang, D. Sapkota, N. N. Hao, L. S. Ling, H. F. Du, L. Pi, C. J. Zhang, D. G. Mandrus, and Y. H. Zhang, *Phys. Rev. B* **96**, 094439 (2017).
- [39] S. C. Haley, S. F. Weber, T. Cookmeyer, D. E. Parker, E. Maniv, N. Maksimovic, C. John, S. Doyle, A. Maniv, S. K. Ramakrishna, A. P. Reyes, J. Singleton, J. E. Moore, J. B. Neaton, and J. G. Analytis, *Phys. Rev. Res.* **2**, 043020 (2020).
- [40] N. J. Ghimire, M. A. McGuire, D. S. Parker, B. Sipos, S. Tang, J. Q. Yan, B. C. Sales, and D. Mandrus, *Phys. Rev. B* **87**, 104403 (2013).
- [41] O. Gorochoy, A. Blanc-soreau, J. Rouxel, P. Imbert, and G. Jehanno, *Philos. Mag. B* **43**, 621 (2006).
- [42] Y. Kousaka, Y. Nakao, J. Kishine, M. Akita, K. Inoue, and J. Akimitsu, *Nucl. Instrum. Methods Phys. Res., Sect. A* **600**, 250 (2009).
- [43] Y. Togawa, J. Kishine, P. A. Nosov, T. Koyama, G. W. Paterson, S. McVitie, Y. Kousaka, J. Akimitsu, M. Ogata, and A. S. Ovchinnikov, *Phys. Rev. Lett.* **122**, 017204 (2019).
- [44] K. T. Ko, K. Kim, S. B. Kim, H. D. Kim, J. Y. Kim, B. I. Min, J. H. Park, F. H. Chang, H. J. Lin, A. Tanaka, and S. W. Cheong, *Phys. Rev. Lett.* **107**, 247201 (2011).
- [45] S. Mankovsky, S. Polesya, H. Ebert, and W. Bensch, *Phys. Rev. B* **94**, 184430 (2016).
- [46] Y. Togawa, Y. Kousaka, K. Inoue, and J. I. Kishine, *J. Phys. Soc. Jpn* **85**, 112001 (2016).
- [47] Y. Liu, Z. X. Hu, E. Stavitski, K. Attenkofer, and C. Petrovic, *Phys. Rev. Res.* **3**, 023181 (2021).
- [48] N. J. Ghimire, A. S. Botana, J. S. Jiang, J. Zhang, Y. S. Chen, and J. F. Mitchell, *Nat. Commun.* **9**, 3280 (2018).
- [49] P. Park, Y. G. Kang, J. H. Kim, K. H. Lee, H. J. Noh, M. J. Han, and J. G. Park, *npj Quantum Mater.* **7**, 42 (2022).
- [50] S. K. Karna, F. N. Womack, R. Chapai, D. P. Young, M. Marshall, W. Xie, D. Graf, Y. Wu, H. Cao, L. DeBeer-Schmitt, P. W. Adams, R. Jin, and J. F. DiTusa, *Phys. Rev. B* **100**, 184413 (2019).
- [51] S. Mangelsen, J. L. Hansen, P. Adler, W. Schnelle, W. G. Bensch, S. Mankovsky, S. Polesya, and H. B. Ebert, *J. Phys. Chem. C* **124**, 24984 (2020).
- [52] J. Dijkstra, P. J. Zijlmat, C. F. van Bruggent, C. Haast, and R. A. de Groot, *J. Phys.: Condens. Matter.* **1**, 6363 (1989).
- [53] S. Mangelsen, P. Zimmer, C. Näther, S. Mankovsky, S. Polesya, H. Ebert, and W. Bensch, *Phys. Rev. B* **103**, 184408 (2021).
- [54] A. C. Bornstein, B. J. Chapman, N. J. Ghimire, D. G. Mandrus, D. S. Parker, and M. Lee, *Phys. Rev. B* **91**, 184401 (2015).